Journal of

Applied and Computational Mechanics

Shahid Chamran
University of Ahvaz

Temperature Effect on Moving Water Droplets at the Channel of PEMFC by Multi-component Multiphase Lattice Boltzmann Method

Mehdi Moslemi[1], Kourosh Javaherdeh[2], Hamid Reza Ashorynejad[3]

[1] Department of Mechanical Engineering, University Campus2, University of Guilan, Rasht, Iran, Email: mehdimoslemi1982@gmail.com

[2] Faculty of Mechanical Engineering, University of Guilan, Rasht, Iran, Email: Javaherdeh@guilan.ac.ir

[3] Imam Khomeini International University-Buin Zahra Higher Education Center of Engineering and Technology, Qazvin, Iran, Email: h.r.ashorynezhad@gmail.com

Abstract. In this paper, a multi-component multiphase pseudopotential Lattice Boltzmann method with multi relaxation time (MRT) collision operator is presented to examine the dynamic behavior of liquid droplets movement and coalescence process in the gas channel of PEMFC. In the numerical method, the forcing term is improved to achieve a high-density ratio and thermodynamic consistency. First, the density ratio, Laplace law, and contact angle are validated with previous studies. Then, different parameters, such as operating temperature, pressure difference, surface contact angle, the radius of droplets, and distance between two droplets on the droplet movement and coalescence process are studied. The results revealed by rising temperature from 30 to 80 degrees, the speed of drop increases around 6 percent. The simulation results indicated that the rising of pressure gradient increases the gas flow velocity on the channel and leads to increasing the shear force and eventually faster movement of the droplet on the gas channel. Also, investigation of various contact angles shows that a hydrophilic surface causes a resistance force between the droplet and the wall and delays the removal of droplets. Moreover, droplet coalescence is useful for droplet movement because of increasing the velocity gradient on top of the droplet; consequently, the shear force on the droplet is raised during coalescence.

Keywords: Lattice Boltzmann method, multi-component multiphase, coalescence process, fuel cell channel, liquid water droplet interaction.

1. Introduction

Nowadays, the study of polymer electrolyte membrane fuel cells (PEMFC) as a power source in vehicles has attracted many researchers attention [1, 2]. Reasons for this tendency include high energy conservation efficiency, low levels of harmful environmental pollutants, low operating temperatures, and relatively rapid onset. Due to the formation of liquid water in the catalyst layer on the cathode side of PEMFC, it is necessary to remove it from the gas channel. The accumulation of liquid water causes flooding in the gas channel and blocking of the oxygen transport pathway, leading to reduced fuel cell efficiency.

Numerous experimental and numerical investigations have been carried out on the removal of liquid water and flooding in the gas channel of the fuel cell [3, 4]. Using neutron radiography measurements, Kramer et al. [5] investigated the two-phase flow phenomena in hydrogen-fueled polymer electrolyte fuel cells (PEFC) by successfully detecting the liquid accumulation in the flow field and gas diffusion layer (GDL) under various operating conditions. Hickner et al. [6] studied the effect of current density and temperature on the water content of an operating proton exchange membrane fuel cell (PEMFC). Using neutron radiography, they found that a peak in water content of the fuel cell was observed at 60°C cell temperature. Kumbur et al. [7] theoretically and experimentally investigated the effect of operational air flow rate, on liquid droplet deformation at the interface of the diffusion media (DM) and the gas flow channel. At high flow rates, removal of liquid water from the DM surface occurs faster, which prevents local channel flooding. Yu et al. [8] experimentally simulated cathode flow channel system with high-sensitivity double parallel conductance probes inspecting system. Hussaini et al. [9] studied the effect of cathode flooding on the operation of the fuel cell. They introduced a new parameter as the wetting area ratio to describe the channel flooding and liquid water coverage on a gas diffusion layer. Zhang et al. [10] presented a liquid water removal from a PEMFC. Their experimental results indicated that there are two major modes of liquid water removal from the GDL surface. First, the droplet detachment by shear forces of gas flow which lead to a mist flow in the gas channel, and second, the capillary wicking onto the more hydrophilic channel, which resulted in the growth of the annular film flow and liquid slug flow in the channel. Rothstein et al. [11] present the effect of contact angle hysteresis on the dynamics of the coalescence of sessile drops. They found that droplet deformation and oscillation during coalescence process are more intensive than that of the single droplet flow.

Due to the limitations of the fuel cell experiment such as deficient to capture more details of dynamic mechanism, considerable researches were conducted on the numerical simulation of liquid water transport behaviors in PEM fuel cell gas

channels which provide more details on the dynamics of water droplet movement in the fuel cell [12-14]. The behavior of the liquid water inside a serpentine channel for a proton exchange membrane (PEM) fuel cell was investigated by Quan et al. [15]. They used the volume of fluid (VOF) numerical method for their simulation. Their results indicated that the bending region of the serpentine flow channel has a significant influence on the flow field and water transport and that flooding may occur after the bend section which might block the transport of reactants inside the flow channel.

Similarly, liquid water transport in the micro-parallel channels with PEM fuel cell stack inlet and outlet was studied by Jiao et al. [16]. They found that excessive and unevenly distributed water in the PEMFC gas channel leads to blocking the airflow or uneven distribution. Zho et al. [17] numerically analyzed the dynamical behavior of water droplets that enter the GDL gas channel using the VOF method. They found that channel height plays an important role in the deformation and detachment of water droplets.

Recently, using the Lattice Boltzmann method as a powerful technique, specifically for the simulation of multi-phase flows has attracted many researchers in the last decade [18-23]. Han et al. [24] also used the Shan-Chen two-phase Lattice Boltzmann model to simulate two liquid droplets growing and moving through a fine pore in the gas channel of a PEM fuel cell. Ben Salah et al. [25] simulated the behavior of water droplets in a gas channel of a PEMFC with multi-phase free energy Lattice Boltzmann model. Their results indicated that increasing droplet velocity and the drainage efficiency in shallow channels occur easier than deep channels; however, the efficiency suddenly decreases when the droplet hits the corner or above the channel's walls. Hao et al. [26] used the Lattice Boltzmann method, to study the emerging of a water droplet through hydrophobic GDL in PEMFC. They realized that the droplet motion on the GDL surface was influenced by the drag shear force of the gas flow. Their results revealed when the velocity of gas flow or contact angle increased water droplet removal is facilitated. Ben Salah et al. [27] utilized the free energy LB model with a high-density ratio to find the optimum GC geometry for water drainage. Their results indicated that a rectangular channel is the best possible geometry for water removal from the gas channel at a reasonable pressure drop. Han and Meng [28] implemented the LB method to simulate the removal of water liquid droplets from two different types of serpentine gas channels. The first one is a smooth U-shaped channel, and the second one has a sharp right angle turning region. Their results indicate that the first type of serpentine gas channel is more suitable for water removal. Additionally, increasing the gas flow velocity or the surface contact angle of the channel can help the process. Ben Amara and Ben Nasrallah [29] simulated the behavior of droplet motion in the gas channel of PEMFC with the single component LB method. They found that increasing capillary number causes more droplet deformation. In addition, the average contact angle of the hysteresis increases along with the droplet motion. Huang and Wu [30] surveyed the dynamic behavior of liquid droplets on the GDL surface. They realized that decreasing the viscosity ratio or increasing the Capillary number leads to easier droplet detachment from the GDL surface.

One of the multi-phase flow modeling in Lattice Boltzmann methods is Shan-Chen pseudopotential method. The main advantages of the pseudopotential method are that the intermolecular interactions are represented with an interaction force based on a density-dependent pseudopotential and the phase separation is naturally achieved by imposing a short-range attraction between different phases. Lue et al[21, 31] implemented pseudopotential Shan-Chen model and improved forcing scheme suggesting for the MRT LB model to achieve thermodynamic consistency and large density ratio in the model. Jiang et al. [32] optimized the method used by Lue et al. [21, 31] to achieve a higher density ratio and a higher Reynolds number. Xu et al. [33] used a pseudopotential LB model to simulate the motion of droplets in a gas channel fuel cell with rough undersurface ,that was simplified to the size of small columns.

In addition, a few studies have been conducted on multi-component systems with high-density ratios [34, 35]. Bao and Schaefer [36] introduced a new multi-component multiphase LBE model which could be simulated with high-density ratio. Zhu et al. [37] incorporated the equation of state into the pseudopotential model and improved it through the MRT model for approximating the collision operator and correction coefficient of K. Hou et al. [38] simulated the dynamics behavior of droplet coalescence in the gas channel of proton exchange membrane fuel cell through a multi-component multi-phase LMB method with high-density ratio. Their results indicated that the shear force strengthened during the droplet coalescence and helped the droplet move from gas channel.

Jitin et al. [39] studied the rate of water removal and the surface area coverage of the gas diffusion layer and the rate of droplet detachment rate in the gas channel of the fuel cell. They showed that the surface coverage of the gas diffusion layer by liquid water could be significantly controlled by the hydrophilic channel walls, although it may reduce the rate of water removal.

The dynamic behavior of liquid droplets on a modified surface of real gas diffusion layer (GDL) with the effect of inertia produced by a three-dimensional (3D) flow channel has been investigated using the lattice Boltzmann model by Yang et al. [40]. The results showed that the liquid droplet is pushed into the gas diffusion layer by the effect of inertia. By increasing the inertia and decreasing the contact angle of the gas diffusion layer, both the penetration depth of the droplet in the gas diffusion layer and the invasion fraction increase.

This study aimed to develop a multi-component multiphase pseudopotential Shan-Chen LB model with multi relaxation time (MRT) collision operator to study the dynamic behavior of coalescence process of liquid droplets in the gas channel of PEMFC.

An important innovation in this paper is the study of the effect of liquid water and gas temperature on droplet motion and their coalescence process, and in the two-phase flow calculation process, a large density difference is established between liquid water and gas in gas channel. One of the significant advantages of this simulation is that it can evaluate actual physical properties, also we used improved pseudopotential multiphase model within lattice Boltzmann model framework, which can realize thermodynamic consistency and tunable surface tension

The real parameters at different temperatures are considered and the conversion of these parameters from physical unit to LB unit is described. In addition, the parameters such as the temperature of components, surface contact angle, Reynolds number, the radius of the droplet, and distance between two droplets are investigated

2. Numerical Method

In this paper, Shan and Chen multi-component multiphase lattice Boltzmann model with multi-relaxation schemes (MRT) are implemented as there are higher stability and accuracy than that of the single relaxation method. In addition, a pseudopotential function is used for considering interparticle interactions in the lattice Boltzmann.

Considering the component k, the collision operator for multi-component multi-phase flows in a 2D lattice can be expressed as below:

$$f_a^k(x + e_a \Delta t, t + \Delta t) - f_a^k(x,t) = -\Omega[f_a^k(x,t) - f_a^{k,eq}(x,t)] + \Delta t S_a^k(x,t) \tag{1}$$

where f_a^k is the density distribution function (DDF) , $f_a^{k,eq}$ is its equilibrium distribution for Component k, Ω is the collision matrix, t is the time, x is the spatial position, Δt is the time step, S_a^k is the forcing term in the velocity space. e_a is the discrete velocity along the ath direction, for the D2Q9 are defined as follows:

$$e_a = \begin{cases} 0 & a = 0 \\ \left(\cos\left[\dfrac{(a-1)\pi}{4}\right], \sin\left[\dfrac{(a-1)\pi}{4}\right]\right) & a = 1,2,3,4 \\ \sqrt{2}\left(\cos\left[\dfrac{(a-1)\pi}{4}\right], \sin\left[\dfrac{(a-1)\pi}{4}\right]\right) & a = 5,6,7,8 \end{cases} \tag{2}$$

The MRT shames offer a higher stability, accuracy, low spurious velocity and achievable density ratio [18, 21, 41-43]. Eq. (1) by MRT method can transformed to the following form:

$$m^{*,k} = m^k - \Lambda\left[m^k(x,t) - m^{eq,k}(x,t)\right] + \Delta t\,(I - 0.5\Lambda)F^k_m \tag{3}$$

where $m^k(x,t)$ and $m^{k,eq}(x,t)$ are vectors of moments and the equilibrium vectors of moments for Component k respectively. M is transformation matrix. The mapping between velocity and moment spaces can be performed by linear transformation.

$$m^k = Mf^k \quad, f = M^{-1}m^k \tag{4}$$

For the D2Q9 lattice, the equilibria m^k and $m^{k,eq}$ can be written as

$$m^k = \left(\rho, e, \varepsilon, j_x, q_x, j_y, q_y, p_{xx}, p_{yy}\right)^T \tag{5}$$

$$m^{k,eq} = \rho\left(1, -2 + 3\left(u_k{}^2 + v_k{}^2\right), 1 - 3\left(u_k{}^2 + v_k{}^2\right), u_k, -u_k, v_k, -v_k, u_k{}^2 - v_k{}^2, u_k v_k\right)^T \tag{6}$$

where Λ is the relaxation matrix and is diagonal in the momentum space:

$$\Lambda = \mathrm{diag}\left(s_1, s_2, s_3, s_4, s_5, s_6, s_7, s_8, s_9\right)$$
$$= \mathrm{diag}\left(\tau_\rho{}^{-1} \quad \tau_e{}^{-1} \quad \tau_\varsigma{}^{-1} \quad \tau_j{}^{-1} \quad \tau_q{}^{-1} \quad \tau_j{}^{-1} \quad \tau_q{}^{-1} \quad \tau_\upsilon{}^{-1} \quad \tau_\upsilon{}^{-1}\right) \tag{7}$$

where the S$_1$, S$_4$ and S$_6$ should be equal to each other and are considered to be one. S$_5$ and S$_7$ equal 1.1 and S$_2$ = S$_3$ and S$_8$ = S$_9$ are related to the bulk and kinematic viscosity, respectively:

$$\lambda = \left(\frac{1}{S_2} - 0.5\right)C_s{}^2 \tag{8}$$

$$\nu = \left(\tau - 0.5\right)C_s^2 \tag{9}$$

where $C_s = 1/\sqrt{3}$ is the lattice sound velocity, and $\tau = 1/s_8$, I is the unit tensor, $(I - 0.5\Lambda)F^k_m$ is the force term in momentum space. Since in the MRT method the relaxation time is related to the kinematic viscosity and at a temperature of $T/T_c = 0.5$, the gas-to-liquid dynamic viscosity ratio is about 25, so we set the relaxation time τ to 1, for the gas phase and from the ratio of kinematic viscosity Calculates relaxation time for liquid phase.

In this paper, to implement the external force into the LB framework, we used Gue's method proposed by Gue et al. [44, 45] and McCracken et al. [43] which is claimed to be derived directly from the Boltzmann equation. In this scheme, the force term in the MRT model should be

$$F^k{}_m = \left[6(u^k F^k{}_x + v^k F^k{}_y), -6(u^k F^k{}_x + v^k F^k{}_y), F^k{}_x, -F^k{}_x, F^k{}_y, -F^k{}_y, 2(u^k F^k{}_x - v^k F^k{}_y), 2(u^k F^k{}_x - v^k F^k{}_y)\right]^T \tag{10}$$

In this model, the density of component and velocity can be expressed as follow [46]:

$$\rho^k = \sum_a f_a \tag{11}$$

$$V^k = \frac{\sum_k\left(\sum_a f_a e_a + \Delta t\,\dfrac{F}{2}\right)}{\sum_k \rho^k} \tag{12}$$

where $F = (F_x, F_y)$ is the total interaction force, acting to the component and express as:

$$F^k = F^k{}_{coh} + F^k{}_{adh} \tag{13}$$

where $F^k{}_{coh}$ is fluid- fluid interaction force defined as follows:

$$F^k{}_{coh} = F^{kk} + F^{kj} \tag{14}$$

where F^{kk} is intra-molecular interaction force and can be written as follows:

$$F^{kk} = -G_{kk}\psi^k(x)C_s{}^2 \sum w\left(|e_\alpha|^2\right)\psi^k(x + e_\alpha)e_\alpha \tag{15}$$

in which $\psi^k(x)$ is the interaction potential, G_{kk} is the interaction strength, and $w(|e_\alpha|^2)$ is the weight operator only that only depends on the length of the length of the vector e_α. It is given by $w(1) = 1/3$ and $w(2) = 1/12$, for the nearest-neighbor interactions on the D2Q9 lattice [47].

The F^{kj} is interaction force between the two components defined in the following [48]:

$$F_{12} = -G_{12}(x)\phi_1(x)\sum_{\alpha=1}^{8} w(|e_\alpha|^2)\phi_2(x + e_\alpha)e_\alpha \tag{16}$$

$$F_{21} = -G_{21}(x)\phi_2(x)\sum_{\alpha=1}^{8} w(|e_\alpha|^2)\phi_1(x + e_\alpha)e_\alpha \tag{17}$$

where $\phi_1(x)$ and $\phi_2(x)$ are different from $\psi^k(x)$ and expressed as:

$$\phi_1(\rho_2) = 1 - \exp\left(\frac{-\rho_2}{-\rho_{20}}\right) \tag{18}$$

$$\phi_2(\rho_1) = a_0 - \exp\left(\frac{-\rho_1}{-\rho_{10}}\right) \tag{19}$$

The value of $\rho_{10}, \rho_{20}, a_0, G_{12}$ and G_{21} are critical for a multicomponent multiphase system [35, 48-50]. Higher values of them lead to the controlling of the magnitude of the mutual diffusivity in the gas phase. In this paper, it is assumed $a_0 = 0.005$, $\rho_{10} = -0.0008 / \log(a_0)$, $\rho_{20} = 0.0003$ [51] and $G_{12} = G_{21} = 0.0001$, F^k_{adh} is fluid-solid adhesion force and calculated by:

$$F^k_{adh}(x) = -G^k_{adh}\psi^k(x)\sum w(|e_\alpha|^2)S(x + e_\alpha \Delta t)e_\alpha \tag{20}$$

where G^k_{adh} is the adhesion factor that determines the strength of the fluid-solid interaction for component k, S is equal to 1 or 0 for a solid and fluid domain node respectively.

Component 1 is water and component 2 is air. The air is considered an ideal fluid and thus $G_{22} = 0$. Water is considered a non-ideal fluid following the Carnahan-Starling (C-S) equation of state, which is given by [52]:

The parameter a effects on the interface thickness,

$$P_{EOS} = \rho RT \frac{1 + b\rho/4 + (b\rho/4)^2 - (b\rho/4)^3}{(1 - b\rho/4)^3} - a\rho^2 \tag{21}$$

where $a = 0.4963R^2T_c^2 / P_c$, $b = 0.8727RT_c / P_c$, and the critical temperature is $T_c = 0.3773a / bR$. In the present study, we set $b = 4$, $R = 1$, $c = 1$. In some previous simulations, a is usually equal to 1 [52], then $T_c = a / (10.601R) \approx 0.094$. But here we use $a = 0.5$ and $T_c \approx 0.047$ same as Li et al. [21]. The parameter a affects the interface thickness, reducing its value causes a thicker interface, which leads to decreased spurious velocity and increased stability in high density ratios. For the water component the effective mass is given by [53]:

$$\psi^1(x) = \sqrt{\frac{2(P_{EOS} - \rho c_s^2)}{G_{11}c_s^2}} \tag{22}$$

In this paper, G_{11} is set to -1 [35]. Also for the air component, the interaction potential is equal to its density [54]. In order to adjust the coexistence densities and surface tension, Li et al. [21] improved the forcing term. Similarly, for the water component, they proposed the following relation for the force term [38]:

$$F^1_m = \begin{bmatrix} 0 \\ 6(uF_x + vF_y) + \frac{12\sigma|F|^2}{\psi^2\delta t(\tau_e - 0.5)} \\ -6(uF_x + vF_y) - \frac{12\sigma|F|^2}{\psi^2\delta t(\tau_e - 0.5)} \\ F_x \\ -F_x \\ F_y \\ -F_y \\ 2(uF_x - vF_y) \\ (uF_y + vF_x) \end{bmatrix} \tag{23}$$

where $|F|^2 = F_x^2 + F_y^2$ and σ is used to achieve good thermodynamic consistency and vary the mechanical stability condition [38].

In the MRT LB equation surface tension cannot be tuned independently due to its relation to density ratio. In order to eliminate the weakness of the multi-range potential, Li and Laue [18] propose an alternative approach to adjust the surface tension of the pseudopotential LB model and added a source term (Eq. (25)) to the right-hand side of the MRT collision equation for a single component. In the present model, we added it in collision MRT equation for water component as follows:

$$m^{*,1} = m^1 - \Lambda\left[m^1(x,t) - m^{1,eq}(x,t)\right] + \Delta t\left(I - \frac{\Lambda}{2}\right)F^1_m + \Delta tC \tag{24}$$

where the source term is expressed as:

$$C = \begin{bmatrix} 0 \\ 1.5\tau_e^{-1}(Q_{xx}+Q_{yy}) \\ -1.5\tau_e^{-1}(Q_{xx}+Q_{yy}) \\ 0 \\ 0 \\ 0 \\ 0 \\ -\tau_v^{-1}(Q_{xx}-Q_{yy}) \\ -\tau_v^{-1}Q_{xy} \end{bmatrix}$$

(25)

The variable Q_{xx}, Q_{yy} and Q_{xy} are given by:

$$Q = KG_{11} / 2\psi^1(x) \sum w(|e_\alpha|^2)(\psi^1(x+e_\alpha)-\psi^1(x))e_\alpha e_\alpha$$

(26)

where the parameter K can adjust the surface tension by its value from 0 to 1 without changing the density ratio, so we have a wider range of surface tension.

It is important to note that in Eq. (24), $m^{*,1}$ can be less than zero. Wu et al. [32] employed a limiter function A_1 with smaller $\tau_e^{-1}, \tau_\varsigma^{-1}$ in relaxation matrix Λ_1 in order to return a MRT collision to this point again, so for component 1 the new $f_a^*(x,t)$ is defined:

$$A_1 : m^{*,1}(x,t+\Delta t)$$
$$\begin{cases} m^1 - \Lambda_1[m^1(x,t)-m^{1,eq}(x,t)] + \Delta t\left(I-\dfrac{\Lambda_1}{2}\right)S + \Delta tC & \text{if } f^{1,*}(x,t+\Delta t) \geq 0 \\ m^1 - \Lambda_1[m^1(x,t)-m^{1,eq}(x,t)] + \Delta t\left(I-\dfrac{\Lambda_1}{2}\right)S + \Delta tC & \text{otherwise} \end{cases}$$

(27)

Subsequently, after A_1 for higher stability, limiter function A_2 is also used as a reserve

$$A_2 : f^{1,*}(x,t+\Delta t)$$
$$\begin{cases} f^{1,*}(x,t+\Delta t) & \text{if } f^{1,*}(x,t+\Delta t) \geq 0 \\ \max\left(0, \dfrac{1}{9}\sum_{i=0}^{8} f^{1,*}(x+e_a\Delta t,t+\Delta t)\right) & \text{if } f^{1,*}(x,t+\Delta t) < 0 \end{cases}$$

(28)

In this paper for relaxation matrix Λ_1, $\tau_e^{-1} = \tau_\varsigma^{-1} = -0.02$.

3. Model Validation

In this section for evaluating Laplace's law a model of the circular droplet with a radius of $r_0 = 40$ is initially placed on the center of the domain. Periodic boundary condition is imposed in the x and y directions. The initial density fields are given as follows:

$$\rho(x,y) = \frac{\rho_l+\rho_g}{2} - \frac{\rho_l-\rho_g}{2}\tanh\left(\frac{2(r-r_0)}{W}\right)$$

(29)

with $r = \sqrt{(x-x_c)^2+(y-y_c)^2}$, where (x_c,y_c) the center of the domain and W is interfacing thickness that is set to 2 lattice units. As well as, ρ_{in} and ρ_{out} are the densities of inside and outside of droplet respectively. The temperature is set to $0.5T_c(T = 50^0C)$, and for the water component the densities are set to $\rho_{out(vap)} = 0.000055$ while for the air component that is set to 5×10^{-7} and 0.000567 for inside and outside of droplet. Also, the grid size is 200×200. After achieving a steady state, the pressure of the system is calculated with [35]:

$$P_{sys} = c_s^2\sum_\sigma \rho_\sigma + \frac{1}{2}c_s^2\sum_\sigma G_{\sigma\sigma}[\psi^\sigma(x)]^2 + \frac{1}{2}c_s^2\sum_{\sigma\neq\bar\sigma}G_{\sigma\bar\sigma}\phi^\sigma(x)\phi^{\bar\sigma}(x)$$

(30)

Laplace's law giving the system pressure difference between inside and outside of droplet is linearly related with the inverse of droplet radius as written in the following:

$$\gamma = \frac{P_{in}-P_{out}}{r}$$

(31)

where P_{in} and P_{out} are respectively the pressure of system inside and outside of the droplet. γ is surface tension and r is the radius of the droplet.

Figure 1 shows the distribution of density for $T/T_c = 0.5$ initial radius $r_0 = 40$ in 200×200 lattice domain and $k = 0.68$. The smoothness in the phase change region and no fluctuation at the interface boundaries indicates that the utilized method is stable and physically justified.
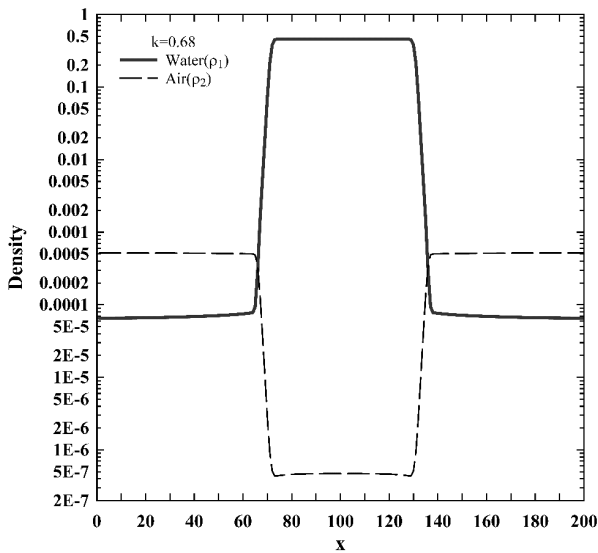
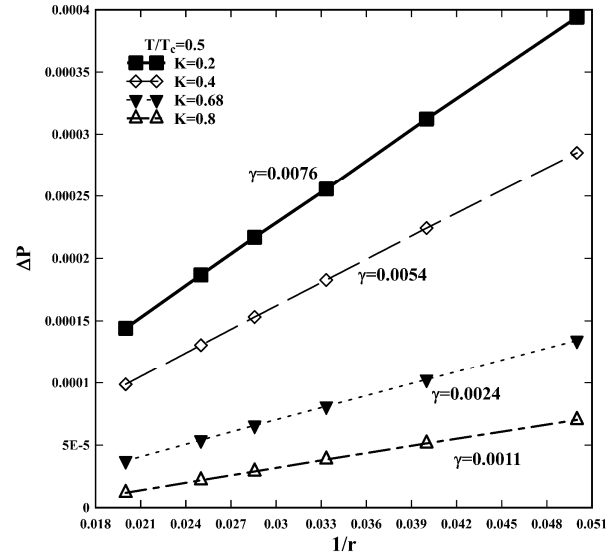**Fig. 1.** Distribution of liquid density for $T/T_c = 0.5$ initial radius $r_0 = 40$.

Fig. 2. Pressure difference and inverse of droplet for validation of the Laplace's law with different value of k at $T/T_c = 0.5$.
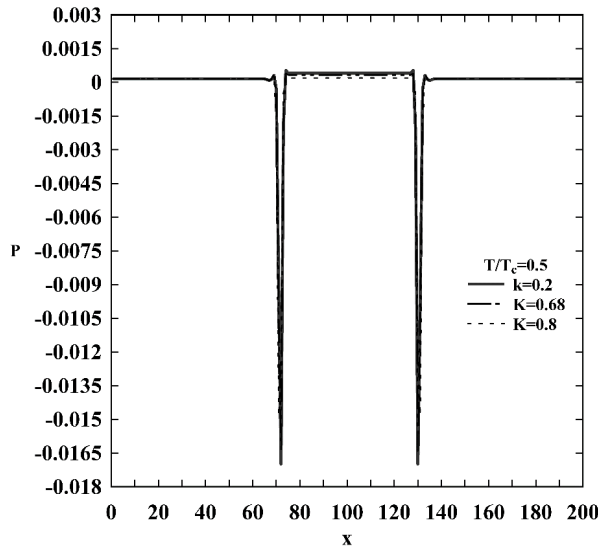

Fig. 3. Pressure distribution along the x direction at $T/T_c = 0.5$.

Figure 2 illustrates the result of simulation at $T/T_c = 0.5$ with different values of K for the validation of Laplace's law. Results demonstrate that by varying the value of K, Numerical results demonstrate that when $k = 0.2$, the amount of surface tension is approximately 8 times when $k = 0.8$, so the proposed approach is able to adjust the surface tension over a wide range with an unchanged density ratio.

The pressure distribution along the x direction of the computational domain for different values of K is shown in Fig. 3. It can be found that large fluctuations of the pressure near the vapor-liquid interface. It is due to a sharp change of density and is ignored in the calculation of ΔP.

The wettability of the surface is determined by the contact angle. If the contact angle is less than 90^0, the surface is hydrophilic and the liquid phase tends to expand as a film on the solid surface. In contrast, if the contact angle is greater than 90^0, the surface is non-wetting or hydrophobic and the liquid phase forms as a droplet on the solid surface. In these simulations, the computational domain is 200×100, Periodic boundary conditions are applied on the left and right edges. The bounce-back boundary condition is applied on the bottom and top solid surfaces. After the simulation is converged, the contact angle is calculated using the expression:

$$\theta = \begin{cases} \arcsin\left(\dfrac{b}{2r}\right) & \theta \leq 90^0 \\ \pi - \arcsin\left(\dfrac{b}{2r}\right) & \theta > 90^0 \end{cases} \tag{32}$$

where r is calculated by
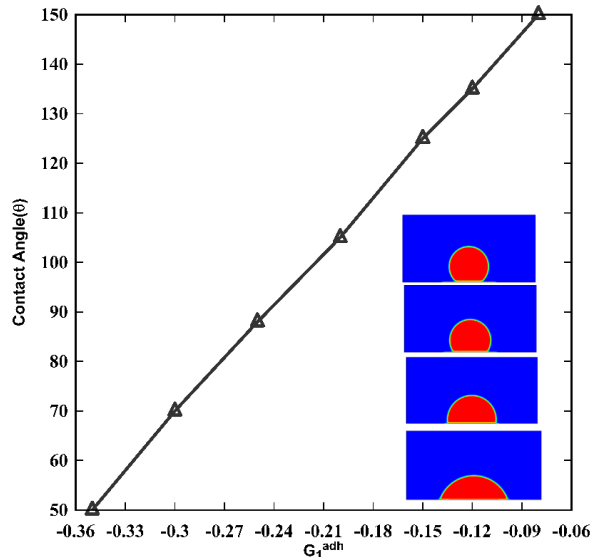
$$r = \frac{4h^2 + b^2}{8h} \tag{33}$$

Fig. 4. Liquid droplet attached to the solid surface in different contact angles at $T/T_c = 0.5$.

in which h and b are the height and base length of the droplet on the surface respectively. Fig. 4 demonstrates a liquid droplet in different contact angles on a solid wall, which indicates an almost linear relationship between the adhesion factor and the contact angle.

4. Simulation Results

The computational domain is a PEMFC gas channel with 2000 μm length and 200 μm height. The bounce-back boundary condition is used for the top and bottom walls. For gas stream flow, constant velocity and convective boundary condition (CBC) [55] are employed at the inlet and outlet of the channel respectively. For the water component, at the inlet, the constant pressure given by Zou-He [56] and at the outlet the CBC are utilized.

Table 1 summarizes the boundary and initial conditions of the gas channel. According to the table, air and water temperatures are between 30 - 80 ^{0}C. Table 2 shows the properties of air and water at different temperatures [57].

For this simulation, the computational domain is discretized using a 2000×200 lattice unit.

The Weber number (We) which represents the competition between the fluid's inertia and surface tension forces acting across an interface between the liquid and gas, or between two immiscible liquids, can be expressed as follows:

$$We = \frac{\rho_d U^2 H}{\gamma} \tag{34}$$

where ρ_d is the fluid density, U is the velocity of air, and γ is the surface tension of water.

The Reynolds number is defined as:

$$Re = \frac{UH}{\upsilon_a} \tag{35}$$

in which H is the height of the gas channel and υ_a is kinematic viscosity of air. According to Laplace's law for different values of K, the amount of surface tension varies. Therefore, to deduce the surface tension of the water in the Lattice Boltzmann unit, the dimensionless parameters of Weber and Reynolds numbers are equal to the real unit and the LBM unit, that the appropriate K from Laplace's law can be selected.

Table 1. Boundary conditions.

Air Inlet	A fully developed laminar velocity profile (mean Vin, air = 2-10 m·s^{-1})
Outlet	Convective Boundary condition
Wall	No slip boundary condition with contact angle θ=87-117 degree
Water and air temperature	30-80 ^{0}C
Gas channel length (L)	2000 μm
Gas channel height (H)	200 μm

Table 2. Water and air properties.

	T=80 ^{0}C	T=50 ^{0}C	T=30 ^{0}C
Dynamic Viscosity of Air (N·s·m^{-2})	2.088×10^{-5}	1.953×10^{-5}	1.865×10^{-5}
Kinematic Viscosity of Air (m^2.s^{-1})	20.88×10^{-6}	17.88×10^{-6}	16.08×10^{-6}
Dynamic Viscosity of water (N·s·m^{-2})	3.537×10^{-4}	5.47×10^{-4}	7.805×10^{-4}
Kinematic Viscosity of water (m^2.s^{-1})	3.64×10^{-7}	5.541×10^{-7}	7.839×10^{-7}
Air-water Surface Tension Coefficient (N.m^{-1})	0.0626	0.0679	0.0712

Table 3. Values of k, lattice unit surface tension and relaxation time for different temperature

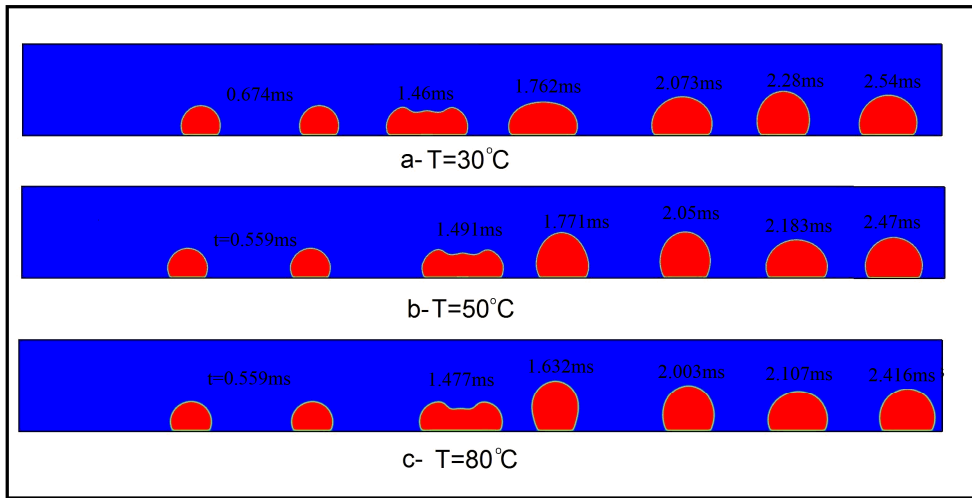|	T=30 ^{o}C	T=50 ^{o}C	T=80 ^{o}C
K	0.5	0.68	0.76
γ	0.00362	0.00242	0.00178
τ_L	0.5244	0.5138	0.5087

Fig. 5. Temperature effect on interaction and coalescence process of two droplet at $D = 300$ μm, $\theta = 117$, $R_1 = R_2 = 55$ μm, $U_{ave} = 8$ m/s.

$$\left(\frac{\rho_d U^2 H}{\gamma}\right)_{Real} = \left(\frac{\rho_d U^2 H}{\gamma}\right)_{LBM} \tag{36}$$

$$\left(\frac{UH}{v_{air}}\right)_{real} = \left(\frac{UH}{v_{air}}\right)_{LBM} \tag{37}$$

where $\mu_d = v_d \cdot \rho_d$ and v_d is kinematic viscosity of droplet. In lattice unit for $T/T_c = 0.5$ we set $v_d = 0.0046$, $v_a = 0.1667$, $\rho_d = 0.4554$ and $H_{Real}/H_{LBM} = 1.0 \times 10^{-6}$, By substituting the U of Reynolds number in the Weber equation the surface tension in LBM unit is obtained. Therefore, the LBM unit surface tension is equal 0.0024 and the appropriate K is equal to 0.68. Table 3 shows the value of k, Lattice unit surface tension, and relaxation time for the liquid phase at different temperatures.

The time step by using Eq. (36) is calculated as follow:

$$\Delta t_{Real} = \left(\frac{\gamma_{LBM}(\mu_d)_{Real}}{\gamma_{Real}(\mu_d)_{LBM}}\right)\Delta x_{Real} \tag{38}$$

This part of the simulation analyses the behavior of motion and coalescence process of two water droplets located at the bottom solid wall of the PEM gas channel. The effect of parameters such as temperature, Reynolds number, surface contact angle, the radius of droplets, and distance between two droplets is investigated. In the current model, the effect of roughness is neglected and a smooth surface is assumed for the walls [17]. The Bond number $(Bo = g(\rho_d - \rho_g)D^2 / \gamma)$ measure the significance of gravitational forces due to density difference compared to surface tension forces. In actual gas channel of PEMFC the Bond number is in order of 10^{-4} and thus the gravitational effect can be neglected. In this study, according to the simulation conditions described in Table 2, the order of Reynolds number is 10^2, the Capillary number and Weber number are in the order of 10^{-2} and 10^{-1} respectively. The values of all of them are similar to the real conditions in the gas channel of PEMFC

Liquid water generated in the catalyst layer passes through the porous GDL and forms a droplet in the gas channel that must be removed. The draining of droplets depends on multi structural and operational parameters such as droplet size, wall contact angle, etc.

Effects of the temperature on liquid droplet interaction are studied. In these three cases, the inlet gas stream velocity is specified at 8.0 ms^{-1}, the distance between droplets (D) is set to 300 μm while the gas stream and droplet temperature are set at 30, 50, and 80 ^{0}C, respectively. Detailed simulation results are presented in Figs. 5-6.

At the temperature of 80 ^{0}C, under a higher surface tension force and also lower kinematic viscosity of air and water the movement of the droplets becomes faster, and they go out of the gas channel quickly around 6 percent.

It is also evident that the effect of shear force on the trailing droplet is greater than that of the leading droplet, so its movement is faster and eventually coalescence process between two droplets happens. After the coalescence process, the height of the drop increases, and the upstream air flow is blocked. Then it causes the maximum velocity on the gap between the droplet and top wall to raise so that ultimately increasing the shear force, making the movement of droplets even faster.

As the temperature enhances, the air-water surface tension force decreases, so the capillary force increases as an important factor in the movement of liquid water in the gas channel. Also, with increasing temperature, the viscosity force, which is a negative factor for the movement of liquid water, decreases, thus accelerating the outflow of water. In Fig. 6, the position of the drop relative to time is shown. It is observed that before the combination, the leading drop has a greater slope than the trailing drop. But after the coalescence process, the slope of the mixing drop is more than any of the two droplets. For the temperature of 80 degrees, the average velocity of the trailing drop is 0.51 m/s and the leading droplet is 0.48 m/s. After the coalescence process,

the average velocity of the droplet is 1.03 m/s, which indicates a more than 115 percent increase in the velocity of the droplet. The results are similar for temperatures of 30 and 50 degrees. It is also clear that with increasing temperature, the coalescence process of the two droplets occurs at a farther distance from the upstream of the gas channel; for example, at the temperature of 80 degrees, the coalescence process occurs in 1.47 ms, while at 50 and 30 degrees those take place at 1.44 ms and 1.4 ms, respectively.

The dynamic motion of the droplets is influenced by Reynolds number. The effect of the Reynolds number on the behavior of the dynamic motion of droplets is displayed in Figs. 7 and 8. In this section, three delicately chosen Reynolds numbers, Re = 250, 300 and 350 are considered at temperatures 50 and 80 degrees. It is known when the Reynolds number is increasing due to an increment in the gas flow velocity, it leads to raising the shear force and pressure difference between both sides of the water droplet and therefore it overcomes the viscosity resistance. The droplets draining become faster more than 1.5 times by 1.5 increase of Reynolds at 50 °C temperature.

It has also been shown that when the temperature rises to 80 °C, a 50% increase in the Reynolds number leads to a 60% rise in the exiting velocity of the droplet from the gas channel.

It is also evident that the effect of shear force on the leading droplet is greater than it on the trailing droplet, so the velocity of the leading droplet is higher especially on greater Re so the coalescence process between two droplets happens rapidly.

It is clear from Fig. 8 that at 50 °C and Reynolds number of 250, the coalescence process occurs in 3.17 ms, whereas with the rise of Reynolds number by 1.4 times, that occurs 1.54 ms earlier, resulting in the droplet exiting faster. By increasing temperature to 80 °C, this effect is slightly reduced; for instance, by raising the Reynolds number from 250 to 350, the coalescence process occurs about 0.85 ms earlier.

Figure 9 illustrate distribution of fluid velocity before and after coalescence process, when the distance between the two droplets is 300 μm and Reynolds number equal 250. It is known that with the coalescence process of the droplets, the gap space at the top of the droplet reduce, the gas flow accelerates and the velocity increases dramatically over there about 50%, so droplet movement is faster about 60% (slope of Fig. 8-a).
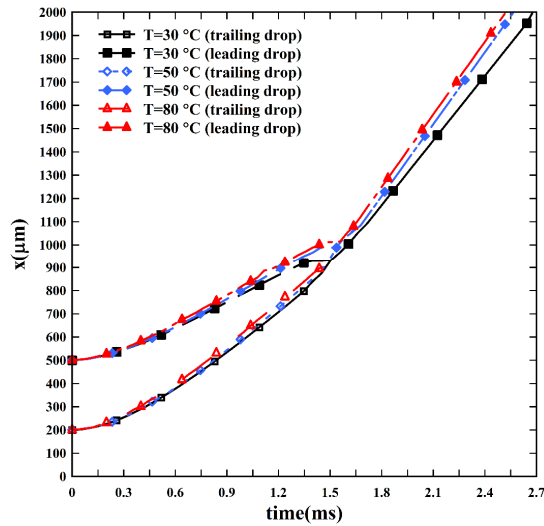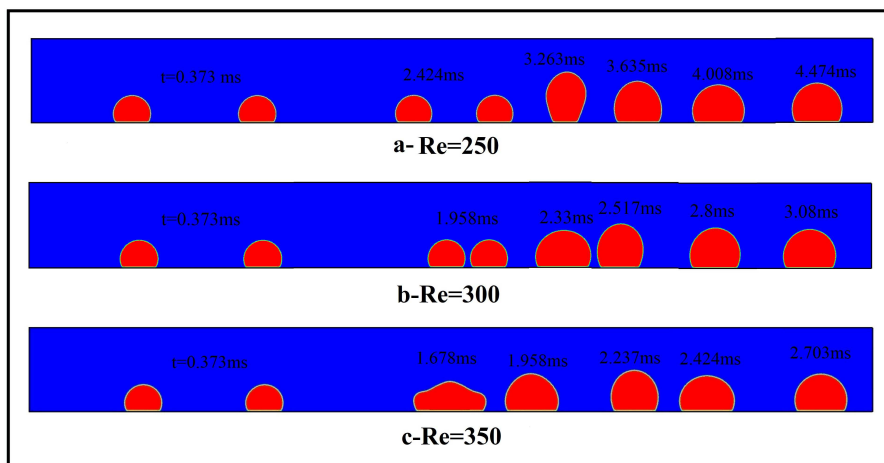

Fig. 6. Position droplet in different temperature.
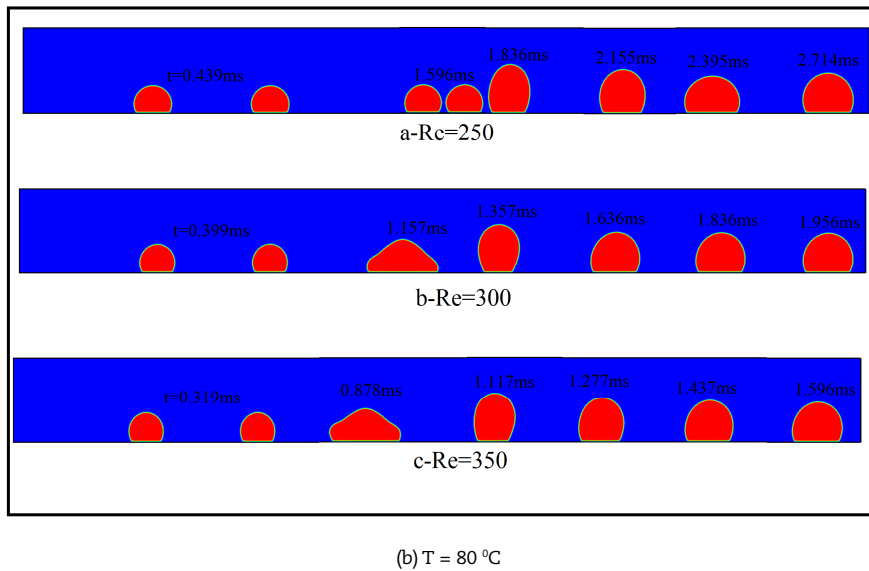

Initial condition

(a) T = 50 °C

(b) T = 80 °C

Fig. 7. Effect Reynolds number on interaction and coalescence process of two droplet at $D = 300$ μm, $\theta = 117$, $R_1 = R_2 = 55$ μm, $T = 50, 80$ °C.
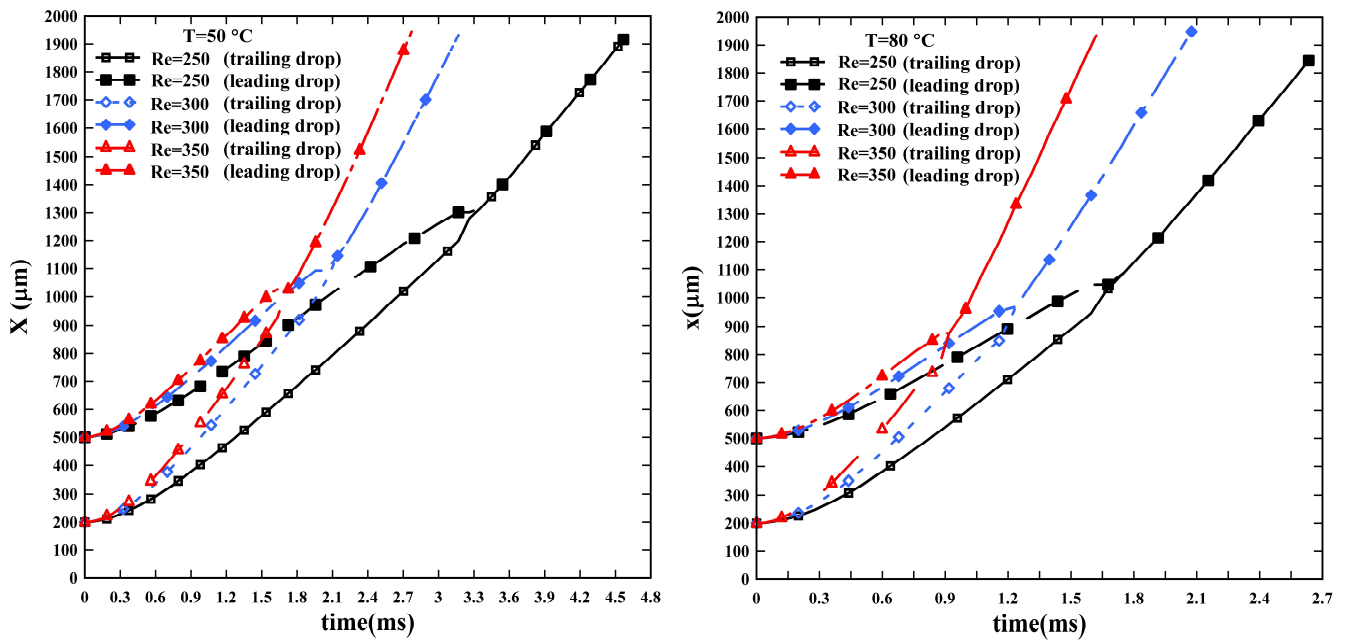

Fig. 8. Position droplet in different Reynolds number at $D = 300$ μm, $\theta = 117$, $R_1 = R_2 = 55$ μm, $T = 50, 80$ °C.

t=0.932ms(Before coalescence process)

t=2.331ms(After coalescence process)
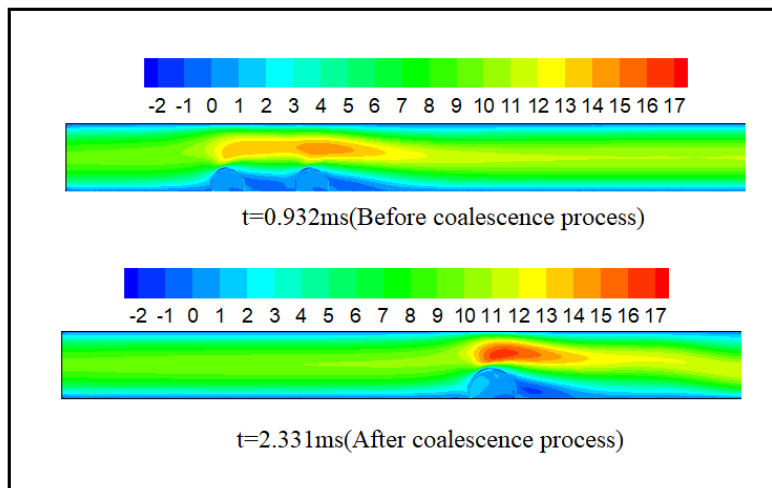
Fig. 9. The distribution of fluid velocity before and after coalescence process at $Re = 300$, $D = 300$ μm, $\theta = 117$, $R_1 = R_2 = 55$ μm, $T = 50$ °C.

Table 4. Parameters in 3 cases.

Case	R_1 (µm)	R_2 (µm)	Distance (µm)
1	70	33.912	300
2	65	42.72	300
3	55	55	300

The larger contact angle would accelerate the droplet motion due to greater shear force, the repulsive force between the water and the wall, and less contact area, thus the separation of the droplet facilitates. The hydrophilic wall plays the role of resistive force between the wall and droplet, reducing the amount of shear force by decreasing its height, and increasing the contact area between the droplet and channel wall, leading to greater resistance which results in delayed droplet draining. Consequently, the droplet motion is faster on the hydrophobic wall. Also, the coalescence process between two droplets occurs farther from the upstream of the gas channel.

This conclusion also works for the gas channel surface as shown in Fig. 10, 11 at contact angles of 87, 107 and 117 degrees. It is clear when the contact angle is 117 degrees, the droplet coalescence process occurs earlier more than 1.5 times relative to the contact angle 87 degrees and closer to the upstream. In Fig. 11, for the contact angle of 117 ^{0}C, the slope of the position-time diagram is greater than the contact angle of 107 ^{0}C and 87 ^{0}C. The average velocity of the leading and trailing droplets at a contact angle of 117 degrees are 0.51 m/s and 0.34 m/s respectively, which after the coalescence process becomes 0.98 m/s, that is approximately more than 1.6 times that of contact angle of 87 degrees. Therefore, at a higher contact angle, the water droplet is removed faster from gas channel. Also, as it is shown in Fig. 11, the coalescence process at a contact angle of 117 degrees is about 1 ms earlier than the contact angle of 87 degrees.

The size of the droplet formed in the gas channel is different and depends on the structural and operational parameters of the fuel cell. In Figs. 12 and 13, the effect of the size of the droplets on its movement along the channel is indicated at temperatures 50 and 80 °C. Table 4 illustrates three different cases where the radius of the two drops is different. Note that the radius of the leading droplet is assumed to be greater than or equal to the radius of the trailing droplet, but the sum of the volume of two droplets is equal in all cases.

It is also evident that the shape of the leading droplet before the coalescence process is similar in all three cases. When the size of this droplet is bigger, the smaller distance between the droplet and top wall, so the higher acceleration and maximum velocity is there and makes the droplet move faster. Simulations showed that at temperatures 50 and 80 °C when the leading droplet radius increases from 55 to 70 µm, the discharge time from the channel decreases by about 20% and 35 % respectively, and also the coalescence process occurs in half time at both temperatures.
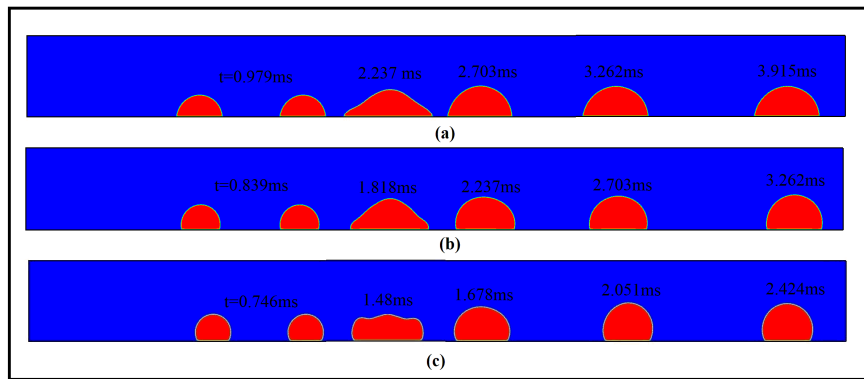

Fig. 10. Effect of the GDL contact angle on interaction and coalescence process of two droplet at D = 300 µm, R_1 = 55 µm, R_2 = 55 µm, and Re = 350 (a) θ = 87, (b) θ = 107, (c) θ = 117.
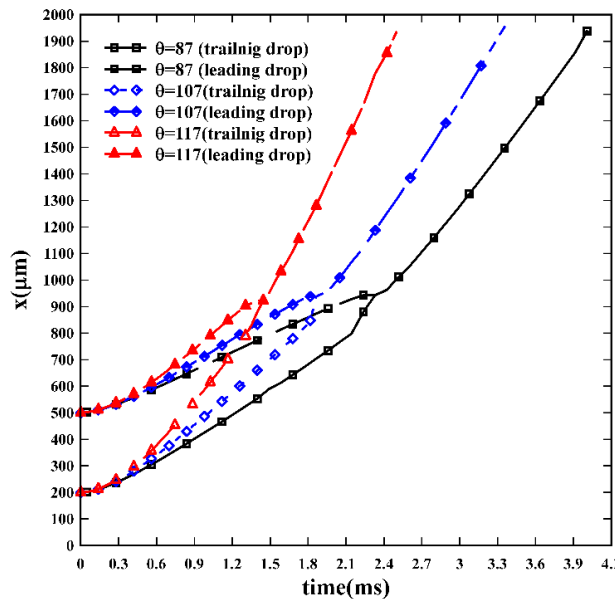

Fig. 11. Position drop in different contact angle at D = 300 µm, R_1 = 55 µm, R_2 = 55 µm, and Re = 350, T = 50°C (a- θ = 87, b- θ = 107, c- θ = 117).

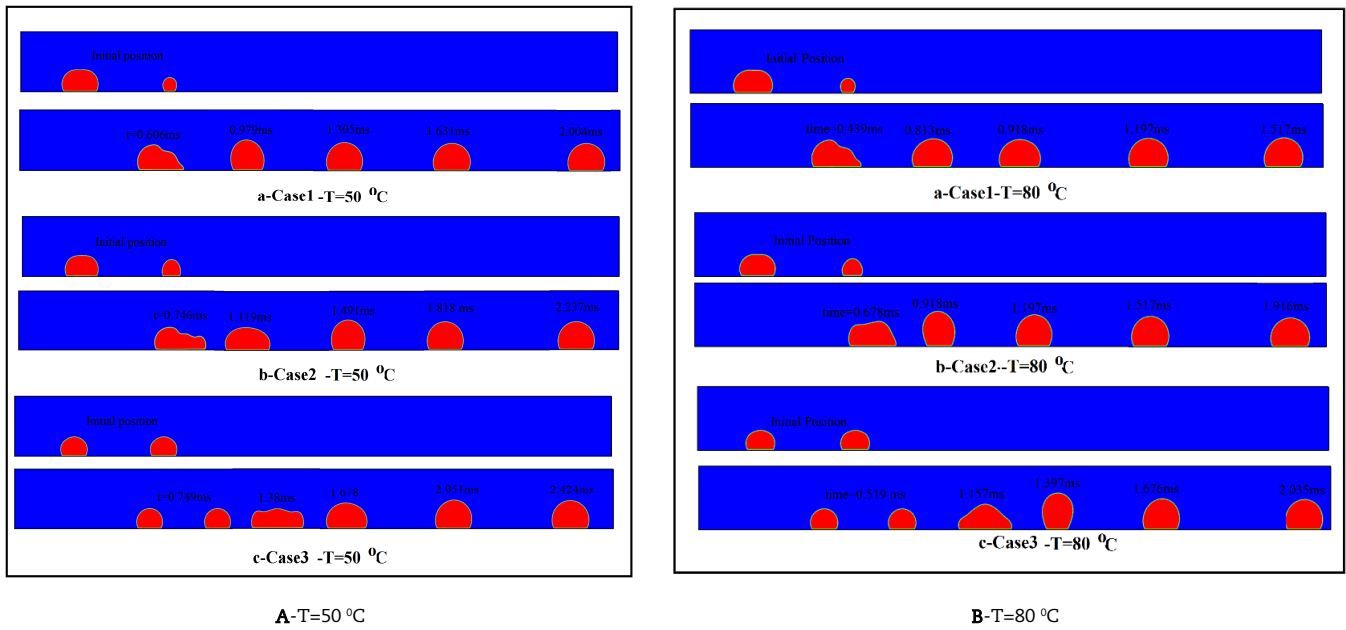**A**-T=50 °C   **B**-T=80 °C

Fig. 12. Effect of the radius of droplet on interaction and coalescence process of two droplet at D = 300 µm, Re = 300, θ = 107, T = 50, 80 °C.
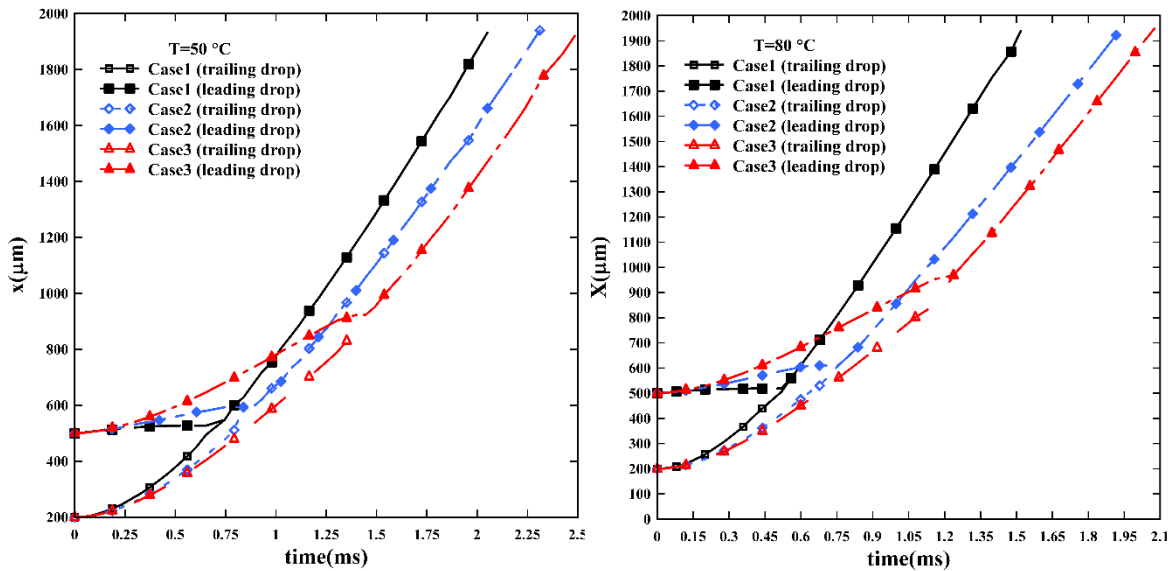
Fig. 13. Position drop in different radius of droplets at D = 300 µm, Re = 300, θ = 107, T = 50, 80 °C.

D = 400 µm

D = 300 µm

D = 200 µm
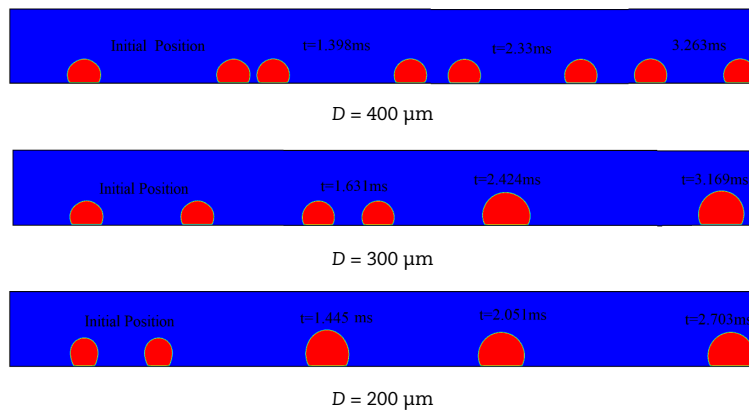
Fig. 14. Effect distance between droplets on interaction and coalescence process at D = 200, 300 and 400 µm, Re = 300, θ = 107, T = 50 °C.

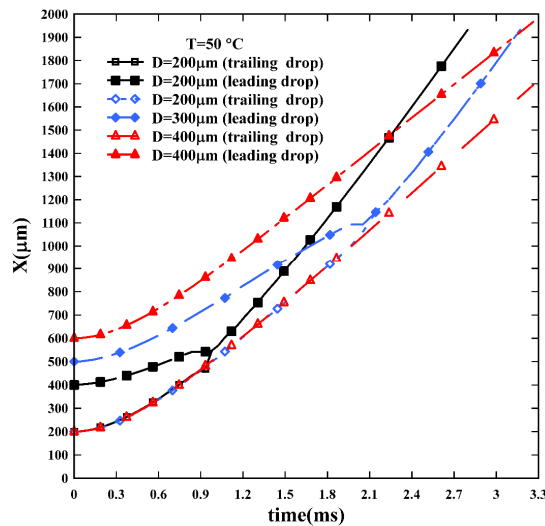**Fig. 15.** Position drop in different distance between at D = 200, 300 and 400 μm, Re = 300, θ = 107, T = 50 ^{0}C.

Due to the complex structure of the GDL, the droplets are formed randomly at different locations, so the distance between them is different. In this section, the effect of the distance between two droplets is studied in Figs. 14 and 15, so that the distance between the two droplets is considered 200, 300 and 400 μm, while in all three cases the Reynolds number is the same.

Results show that when the distance between the two droplets is 200 μm the drag shear force on the trailing droplet is reduced, so the leading droplet hits the trailing droplet faster and the coalescence process is taken place. After that, the radius of the droplet becomes bigger and the gap between the droplet and the top wall of the gas channel decreases, so the fluid accelerates and velocity of the air component increase thus the drag shear force enhances; as a result, the droplet movement becomes faster. In general, it can be found that the coalescence process is beneficial for the exiting droplet from the channel.

Before droplet fusion, when the distance between two drops is 200 μm, the average velocity of the trailing drop is at most 60% of the leading drop. So, the leading drop reaches the trailing drop faster and the coalescence process is done. Although, when the distance between the two drops increases to 400 μm, the average velocity of the trailing drop is at least 90% of the average velocity of the leading drop. Therefore, the coalescence operation does not take place and only the distance between the two droplets is reduced at the end of the channel by about 30% and each droplet leaves the channel separately.

5. Conclusion

A numerical investigation on the interaction and coalescence process of two water droplets in a gas channel of PEMFC was presented using multi-component multiphase pseudopotential Lattice Boltzmann method with multi relaxation time (MRT) collision operator.

In this way, two droplets were placed inside the gas channel and their movement and coalescence process were studied under different parameters such as temperature, contact angle, Reynolds number, radius of droplets, and the distance between them.

Important findings and conclusions are summarized in the following.

1. When the temperature of gas flow and drops increases, the kinematic viscosity decreases which leads the droplets to exit faster from the gas channel.
2. Increasing the Reynolds number causes the shear force to increase, as a result, the droplet movement and merging accelerate.
3. Our simulations demonstrate the effects of wall wettability on the removal and coalescence process of droplets, showing that on a more hydrophobic surface due to a higher repulsive force between the wall and the droplet, the motion of droplet is faster.
4. For the same air velocity and total droplet volume, with a larger diameter of trailing drop, water withdrawal from the microchannel is significantly quick.
5. Decreasing the distance between two droplets reduces the shear drag force applied to the trailing droplet, thus the trailing droplet hits the leading droplet faster and merges with it. Also, results demonstrated that when the distance between two droplets increases to 400 micrometers, each droplet exits the channel separately.

Author Contributions

Acknowledgments

Conflict of Interest

This is the original work of the authors and all authors have seen and approved the final version of the manuscript being submitted. The material described here is not under publication or consideration for publication elsewhere.

Funding

Data Availability Statements

The datasets generated and/or analyzed during the current study are available from the corresponding author on reasonable request.

Nomenclature

a	Parameter in EOS	w	Weight coefficient
b	Parameter in EOS	x	Lattice site; direction
C_s	Lattice sound speed	y	Direction
Ca	Capillary number		
D	Distance between droplets	**Greek letters**	
e	Discrete velocity	γ	Surface tension
f	Distribution function, frequency	μ	Dynamic viscosity
F	Total interaction force	θ	Contact angle
F_{adh}	Fluid-solid adhesion force	λ	Bulk viscosity
F_{coh}	Fluid-fluid interaction	Λ	Diagonal relaxation matrix
H	Height of gas channel	ρ	Density
I	Unit tensor	σ	Thermodynamic consistency parameter
K	Surface tension adjustment parameter	τ	Relaxation time
K	Tuned a surface tension	υ	Kinematic viscosity
m	Distribution function at moment space	ψ	Interaction potential
M	Transformation matrix	ω	Weight coefficient
p	Pressure	Ω	Collision matrix
Q	Variables to tune surface tension		
R	Universal gas constant;	**Subscripts and superscripts**	
Re	Reynolds number	1	Water component
r	Radius of droplet	2	Air component
S	Forcing term	a	Air
t	Time (ms)	adh	Adhesion force
T	Temperature	c	Critical point
u	Velocity in x direction	d	Droplet
v	Velocity in y direction	eq	Equilibrium distribution
		EOS	Equation of state

References

[1] Wu, J., X.Z. Yuan, J.J. Martin, H. Wang, J. Zhang, J. Shen, S. Wu, and W. Merida, A review of PEM fuel cell durability: Degradation mechanisms and mitigation strategies, *Journal of Power Sources*, 184(1), 2008, 104-119.

[2] Jiao, K. and M. Ni, Challenges and opportunities in modelling of proton exchange membrane fuel cells (PEMFC), 2017.

[3] Jiao, K. and X. Li, Water transport in polymer electrolyte membrane fuel cells, *Progress in Energy and Combustion Science*, 37(3), 2011, 221-291.

[4] Yousfi-Steiner, N., P. Moçotéguy, D. Candusso, D. Hissel, A. Hernandez, and A. Aslanides, A review on PEM voltage degradation associated with water management: Impacts, influent factors and characterization, *Journal of Power Sources*, 183(1), 2008, 260-274.

[5] Kramer, D., J. Zhang, R. Shimoi, E. Lehmann, A. Wokaun, K. Shinohara, and G.G. Scherer, In situ diagnostic of two-phase flow phenomena in polymer electrolyte fuel cells by neutron imaging: Part A. Experimental, data treatment, and quantification, *Electrochimica Acta*, 50(13), 2005, 2603-2614.

[6] Hickner, M.A., N. Siegel, K. Chen, D. McBrayer, D.S. Hussey, D.L. Jacobson, and M. Arif, Real-time imaging of liquid water in an operating proton exchange membrane fuel cell, *Journal of The Electrochemical Society*, 153(5), 2006, A902-A908.

[7] Kumbur, E., K. Sharp, and M. Mench, Liquid droplet behavior and instability in a polymer electrolyte fuel cell flow channel, *Journal of Power Sources*, 161(1), 2006, 333-345.

[8] Yu, L.-J., W.-C. Chen, M.-J. Qin, and G.-P. Ren, Experimental research on water management in proton exchange membrane fuel cells, *Journal of Power Sources*, 189(2), 2009, 882-887.

[9] Hussaini, I.S. and C.-Y. Wang, Visualization and quantification of cathode channel flooding in PEM fuel cells, *Journal of Power Sources*, 187(2), 2009, 444-451.

[10] Zhang, F., X. Yang, and C. Wang, Liquid water removal from a polymer electrolyte fuel cell, *Journal of the Electrochemical Society*, 153(2), 2006, A225-A232.

[11] Nilsson, M.A. and J.P. Rothstein, The effect of contact angle hysteresis on droplet coalescence and mixing, *Journal of Colloid and Interface Science*, 363(2), 2011, 646-654.

[12] Hou, Y., G. Zhang, Y. Qin, Q. Du, and K. Jiao, Numerical simulation of gas liquid two-phase flow in anode channel of low-temperature fuel cells, *Internatio6nal Journal of Hydrogen Energy*, 42(5), 2017, 3250-3258.

[13] Zhu, X., P. Sui, and N. Djilali, Three-dimensional numerical simulations of water droplet dynamics in a PEMFC gas channel, *Journal of Power Sources*, 181(1), 2008, 101-115.

[14] Kim, H.-Y., S. Jeon, M. Song, and K. Kim, Numerical simulations of water droplet dynamics in hydrogen fuel cell gas channel, *Journal of Power Sources*, 246, 2014, 679-695.

[15] Quan, P., B. Zhou, A. Sobiesiak, and Z. Liu, Water behavior in serpentine micro-channel for proton exchange membrane fuel cell cathode, *Journal of Power Sources*, 152, 2005, 131-145.

[16] Jiao, K., B. Zhou, and P. Quan, Liquid water transport in straight micro-parallel-channels with manifolds for PEM fuel cell cathode, *Journal of Power Sources*, 157(1), 2006, 226-243.

[17] Zhu, X., P. Sui, and N. Djilali, Dynamic behaviour of liquid water emerging from a GDL pore into a PEMFC gas flow channel, *Journal of Power Sources*, 172(1), 2007, 287-295.

[18] Li, Q., K.H. Luo, Q. Kang, Y. He, Q. Chen, and Q. Liu, Lattice Boltzmann methods for multiphase flow and phase-change heat transfer, *Progress in Energy and Combustion Science*, 52, 2016, 62-105.

[19] Chen, L., Q. Kang, Y. Mu, Y.-L. He, and W.-Q. Tao, A critical review of the pseudopotential multiphase lattice Boltzmann model: Methods and applications, *International Journal of Heat and Mass Transfer*, 76, 2014, 210-236.

[20] Li, M., C. Huber, Y. Mu, and W. Tao, Lattice Boltzmann simulation of condensation in the presence of noncondensable gas, *International Journal of Heat and Mass Transfer*, 109, 2017, 1004-1013.

[21] Li, Q., K. Luo, and X. Li, Lattice Boltzmann modeling of multiphase flows at large density ratio with an improved pseudopotential model, *Physical Review E*, 87(5), 2013, 053301.

[22] Qian, Y.-H., D. d'Humières, and P. Lallemand, Lattice BGK models for Navier-Stokes equation, *EPL (Europhysics Letters)*, 17(6), 1992, 479.

[23] Huang, H., Z. Li, S. Liu, and X.Y. Lu, Shan-and-Chen-type multiphase lattice Boltzmann study of viscous coupling effects for two-phase flow in porous media, *International Journal for Numerical Methods in Fluids*, 61(3), 2009, 341-354.

[24] Han, B., J. Yu, and H. Meng, Lattice Boltzmann simulations of liquid droplets development and interaction in a gas channel of a proton exchange membrane fuel cell, *Journal of Power Sources*, 202, 2012, 175-183.

[25] Salah, Y.B., Y. Tabe, and T. Chikahisa, Two phase flow simulation in a channel of a polymer electrolyte membrane fuel cell using the lattice Boltzmann method, *Journal of Power Sources*, 199, 2012, 85-93.

[26] Hao, L. and P. Cheng, Lattice Boltzmann simulations of liquid droplet dynamic behavior on a hydrophobic surface of a gas flow channel, *Journal of Power Sources*, 190(2), 2009, 435-446.

[27] Salah, Y.B., Y. Tabe, and T. Chikahisa, Gas channel optimisation for PEM fuel cell using the lattice Boltzmann method, *Energy Procedia*, 28, 2012, 125-133.

[28] Han, B. and H. Meng, Lattice Boltzmann simulation of liquid water transport in turning regions of serpentine gas channels in proton exchange membrane fuel cells, *Journal of Power Sources*, 217, 2012, 268-279.

[29] Amara, M.E.A.B. and S.B. Nasrallah, Numerical simulation of droplet dynamics in a proton exchange membrane (PEMFC) fuel cell micro-channel, *International Journal of Hydrogen Energy*, 40(2), 2015, 1333-1342.

[30] Wu, J. and J.-J. Huang, Dynamic behaviors of liquid droplets on a gas diffusion layer surface: Hybrid lattice Boltzmann investigation, *Journal of Applied Physics*, 118(4), 2015, 044902.

[31] Li, Q., K.H. Luo, and X. Li, Forcing scheme in pseudopotential lattice Boltzmann model for multiphase flows, *Physical Review E*, 86(1), 2012, 016709.

[32] Wu, Y., N. Gui, X. Yang, J. Tu, and S. Jiang, Improved stability strategies for pseudo-potential models of lattice Boltzmann simulation of multiphase flow, *International Journal of Heat and Mass Transfer*, 125, 2018, 66-81.

[33] Xu, A., T. Zhao, L. An, and L. Shi, A three-dimensional pseudo-potential-based lattice Boltzmann model for multiphase flows with large density ratio and variable surface tension, *International Journal of Heat and Fluid Flow*, 56, 2015, 261-271.

[34] Stiles, C.D. and Y. Xue, High density ratio lattice Boltzmann method simulations of multicomponent multiphase transport of H2O in air, *Computers & Fluids*, 131, 2016, 81-90.

[35] Chen, L., Q. Kang, Q. Tang, B.A. Robinson, Y.-L. He, and W.-Q. Tao, Pore-scale simulation of multicomponent multiphase reactive transport with dissolution and precipitation, *International Journal of Heat and Mass Transfer*, 85, 2015, 935-949.

[36] Bao, J. and L. Schaefer, Lattice Boltzmann equation model for multi-component multi-phase flow with high density ratios, *Applied Mathematical Modelling*, 37(4), 2013, 1860-1871.

[37] Zhu, W., M. Wang, and H. Chen, Study on multicomponent pseudo-potential model with large density ratio and heat transfer, *International Communications in Heat and Mass Transfer*, 87, 2017, 183-191.

[38] Hou, Y., H. Deng, Q. Du, and K. Jiao, Multi-component multi-phase lattice Boltzmann modeling of droplet coalescence in flow channel of fuel cell, *Journal of Power Sources*, 393, 2018, 83-91.

[39] Jithin, M., M.K. Das, and A. De, Phase Field Lattice Boltzmann Simulations of Water Droplet Transport in a Proton Exchange Membrane Fuel Cell Flow Channel, *International Journal of Energy for a Clean Environment*, 22(3), 2021, 43-76.

[40] Yang, J., L. Fei, X. Zhang, X. Ma, K.H. Luo, and S. Shuai, Dynamic behavior of droplet transport on realistic gas diffusion layer with inertial effect via a unified lattice Boltzmann method, *International Journal of Hydrogen Energy*, 46(66), 2021, 33260-33271.

[41] Yu, Z. and L.-S. Fan, Multirelaxation-time interaction-potential-based lattice Boltzmann model for two-phase flow, *Physical Review E*, 82(4), 2010, 046708.

[42] Succi, S., *The lattice Boltzmann equation: for fluid dynamics and beyond*, Oxford University Press, 2011.

[43] McCracken, M.E. and J. Abraham, Multiple-relaxation-time lattice-Boltzmann model for multiphase flow, *Physical Review E*, 71(3), 2005, 036701.

[44] Guo, Z. and C. Zheng, Analysis of lattice Boltzmann equation for microscale gas flows: relaxation times, boundary conditions and the Knudsen layer, *International Journal of Computational Fluid Dynamics*, 22(7), 2008, 465-473.

[45] Zheng, L., B. Shi, and Z. Guo, Multiple-relaxation-time model for the correct thermohydrodynamic equations, *Physical Review E*, 78(2), 2008, 026705.

[46] Sega, M., M. Sbragaglia, S.S. Kantorovich, and A.O. Ivanov, Mesoscale structures at complex fluid–fluid interfaces: a novel lattice Boltzmann/molecular dynamics coupling, *Soft Matter*, 9(42), 2013, 10092-10107.

[47] Sbragaglia, M., R. Benzi, L. Biferale, S. Succi, K. Sugiyama, and F. Toschi, Generalized lattice Boltzmann method with multirange pseudopotential, *Physical Review E*, 75(2), 2007, 026702.

[48] Yu, Z., X. Shan, and L. Fan. An improved multi-component lattice Boltzmann method for simulation of gas–liquid flows with high density ratio, *AICHE Annual Meeting*, 2007.

[49] Liu, M., Z. Yu, T. Wang, J. Wang, and L.-S. Fan, A modified pseudopotential for a lattice Boltzmann simulation of bubbly flow, *Chemical Engineering Science*, 65(20), 2010, 5615-5623.

[50] Shan, X., Analysis and reduction of the spurious current in a class of multiphase lattice Boltzmann models, *Physical Review E*, 73(4), 2006, 047701.

[51] Yu, Z., A novel lattice Boltzmann method for direct numerical simulation of multiphase flows, The Ohio State University, 2009.

[52] Yuan, P. and L. Schaefer, Equations of state in a lattice Boltzmann model, *Physics of Fluids*, 18(4), 2006, 042101.

[53] Hu, A., L. Li, S. Chen, Q. Liao, and J. Zeng, On equations of state in pseudo-potential multiphase lattice Boltzmann model with large density ratio, *International Journal of Heat and Mass Transfer*, 67, 2013, 159-163.

[54] Sbragaglia, M. and D. Belardinelli, Interaction pressure tensor for a class of multicomponent lattice Boltzmann models, *Physical Review E*, 88(1), 2013, 013306.

[55] Yang, Z., Lattice Boltzmann outflow treatments: Convective conditions and others, *Computers & Mathematics with Applications*, 65(2), 2013, 160-171.

[56] Zou, Q. and X. He, On pressure and velocity boundary conditions for the lattice Boltzmann BGK model, *Physics of Fluids*, 9(6), 1997, 1591-1598.

[57] Kim, J.H. and W.T. Kim, Numerical investigation of gas-liquid two-phase flow inside PEMFC gas channels with rectangular and trapezoidal cross sections, *Energies*, 11(6), 2018, 1403.

ORCID iD

Mehdi Moslemi https://orcid.org/0000-0002-1570-011X
Kourosh Javaherdeh https://orcid.org/0000-0002-0572-9592
Hamid Reza Ashorynejad https://orcid.org/0000-0002-3416-0112